Design and in field validation of a modular metamaterial for mitigation of railway induced vibrations

Design and in field validation of a modular metamaterial for mitigation of railway induced vibrations

F. Nistri, F. Bosia, A. Gliozzi

Department of Applied Science and Technology, Politecnico di Torino, C.so Duca degli Abruzzi, 24 - 10129 Torino (Italy)

L. D'Alessandro, S. Caverni, P. Charkaluk

Phononic Vibes s.r.l., Via Simone Schiaffino, 11 - 20158 Milano (Italy)

A. Corigliano

Department of Civil and Environmental Engineering, Politecnico di Milano, Piazza Leonardo da Vinci, 32 - 20133 Milano (Italy)

M. Miniaci

CNRS, Centrale Lille, ISEN, Univ. Lille, Univ. Valenciennes, UMR 8520 - IEMN, Villeneuve-D'Ascq - 60069 (France)

A. Colombi

Department of Civil, Environmental and Geomatic Engineering, ETH Zürich, Wolfgang-Pauli-Str. 27 - 8093 Zürich (Switzerland)

N. Pugno

Laboratory for Bioinspired, Bionic, Nano, Meta Materials Mechanics, Department of Civil, Environmental and Mechanical Engineering, University of Trento, Trento, 38123 Italy

---

Abstract

Metamaterials are artificial structures exhibiting wave control properties that can be exploited in civil engineering applications. Among them, locally resonant metamaterials are able to control and manipulate wave propagation at wavelengths several times larger than the unit cell size, and can therefore be useful for low frequency vibration suppression. This paper presents the design, installation and validation of a 0.4 m thick metamaterial-based panel

for mitigation of railway-induced vibrations. The barrier comprises a cubic locally resonating unit made of four concrete pyramids connected together by external slender steel rebars. The unit cell is characterized from the dynamic point of view both numerically and experimentally, and a full-scale field test is then performed on the barrier at the railway station in Elze (Germany). This test validates the effectiveness of the metamaterial-based panel in providing a low frequency mitigation of 10 dB at the resonance frequency around 30 Hz, in good agreement with the numerical and laboratory tests.

Keywords: Metamaterials, trench barrier, railway-induced vibrations, in-situ experiment

1. Introduction

In recent years, growing concern over the detrimental effects of seismic wave and groundborne vibrations has prompted significant research efforts aimed at mitigating these phenomena. In particular, vibrations induced by railways pose a significant impact on both the built environment and residents, manifesting themselves as Rayleigh waves propagating at the soil surface. The generation of these surface waves is described in [1], where state-of-the-art mitigation solutions, including trench barriers, are compared. In this context, [2] presented Finite Element (FE) simulations to explore the effectiveness of a robust concrete trench barrier installed near a traditional railway line, subsequently validating the findings through in-field testing. Another strategy, outlined in [3], involved the deployment of buried steel sheet piles, with both numerical simulations and experimental testing conducted in the relevant environment.

A recently developed technology that can help to address this problem is that of MetaMaterials (MM), whose study and development has gained increasing attention, due to the possibility of achieving unprecedented material performance in many fields, such as vibration [4, 5, 6] and noise control [7]. First developed in electromagnetism and optoelectronics [8], MMs are defined as artificially structured materials characterized by macroscopic properties that would not be typical of the raw material they are made of. Among these, so-called phononic crystals (PnC) exploit the repetition of a Unit Cell (UC) and the Bragg scattering phenomenon to suppress the propagation of the mechanical waves in specific frequency ranges through the creation of band gaps. Thus, it is possible to create band-gaps targeting specific wavelengths

that are comparable with the size of the UC. Another means to create band gaps is to use locally resonant metamaterials, which are instead obtained by a periodic or non-periodic arrangement of resonators, whose resonance frequency depends only on their inertia and restoring force. This allows to create bandgaps at frequencies corresponding to wavelengths several times larger than the UCs [9, 10]. In some cases, the band gaps due to Bragg scattering and local resonance can coincide [11]. Other coupling effects such as multiple Bragg wave coupling, veering and locking can take place, locally modifying the dispersion of the waves [12, 13, 14].

Numerous investigations have explored the potential use of MM in mitigating seismic vibrations. Numerical studies have focused on metamaterial-based trench barriers, investigating the geometry and material dependencies of phononic crystal and locally resonant barriers, respectively. [15, 16]. In [17], researchers employed an array of buried resonators near the surface as a seismic metabarrier. The system, constructed employing commonly used materials such as a concrete case and a steel cylinder suspended by elastic bearings, was modelled numerically and then verified in a scaled-down experimental setup. Similarly, the effect of buried resonators or periodic cavities was studied in [18]. In [19], a numerical study on an array of buried pillar resonator clamped to a bedrock demonstrated the possibility of achieving bangaps in the 1-10 Hz range for seismic protection. Further theoretical work on seismic protection was developed in [20], studying the propagation of a Rayleigh wave on half space with an array of rod resonators. In [21], the application of a graded array of rods on an elastic substrate was used to generate Rayleigh wave rainbow trapping and mode conversion, redirecting the propagation form the surface to the bulk. Furthermore, [22],] examined the influence of natural resonators, such as trees and forests, revealing through field tests that Rayleigh waves, propagating in soft sedimentary soil at frequencies below 80 Hz, exhibited substantial attenuation by these natural resonators.

In this paper, MM vibration mitigation properties are exploited to address this critical problem. Starting from the UC geometry developed in [23, 24], a MM based barrier with a low resonance frequency is designed for applications in railway-induced vibrations, in particular to address Rayleigh waves, which propagate at the surface. The process of design and validation of the MM panel for railway-induced vibration mitigation is thus presented. Firstly, a detailed description of the UC is given in Section 2. Its numerical analysis is then described in Section 3 and compared with experimental results in

Section 4. Section 5 subsequently explains the design of the anti-vibration modules, composed of U-shaped blocks enclosing the designed UCs and Section 6 illustrates their numerical characterization. Finally, in Section 7, the experimental campaign on the field is described along with the corresponding results to validate the effectiveness of the MM panel. Closing remarks are provided in Section 8.

2. Unit Cell Design

The first objective of this work is the design and the dynamic characterization of a MM UC working at subwavelength range, which could be used as fundamental unit for a barrier for railway-induced vibration mitigation in soil. The proposed UC structure is based on previous studies [24, 23] and chosen in order to both maximize the participating mass and minimize the stiffness as well as to tune the vibration damping properties in the low frequency range. Due to their design of thin beams and large masses, the modes featuring larger modal mass of the system (pyramids) are confined in the low passbands, while the ones featuring smaller modal mass (beams) are confined in the high passband, in what is known as mode separation [24, 23]. A 3D view of the proposed UC is shown in Figure 1a. The main dimensions of the UC, made of 6 pyramids disposed symmetrically, are illustrated in Figure 1b in a mid cross section view, where the main side of the cubic cell is assumed to be $a_{cell} = 0.36\,m$, while the pyramid side is $l_{pyr} = 0.30\,m$.

The materials chosen for the fabrication of the UCs are steel and concrete. The presence of fibres in the concrete mix increases its overall tensile, shear, and compressive strength, and is required to avoid using rebars as reinforcement in the pyramids, given the limited available volume. Although this is not strictly necessary for the operating phase, where no payloads are supported, it can be important for the installation phase, where impacts can occur.

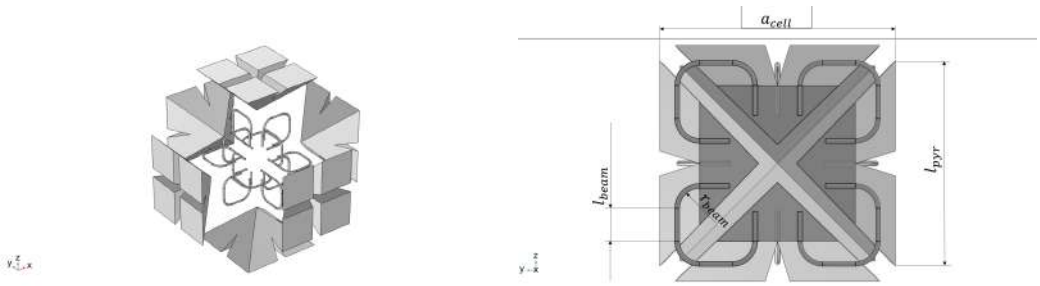

(a) (b)

Figure 1: Structures of the UC: (a) Exploded 3D view (b) Section view with details of the connections between steel beams and concrete pyramids.

Each pyramid is connected to the neighbouring ones through an L-shaped steel beams. Each beam presents hooks on both ends in order to strengthen the attachment the bond between beams and pyramidal elements. These are made of stainless steel AISI 630, have an 8 mm diameter circular section and are curved at 90^o (with a total bending radius equal to 4.5 times the diameter of the beam).

3. UC Numerical Analysis

The dynamic behaviour of the chosen unit cell is first analysed numerically. Dispersion analysis is performed, investigating the potential behaviour for an infinite array of unit cells. Then, a modal analysis of the single cell is carried out.

3.1. Dispersion analysis of the single cell

Simulations are performed using the FE Method, in particular by means of the Structural Mechanics Module of COMSOL Multiphysics. The pyramids are modelled by means of solid tetrahedral elements, with the element size adapted to the geometrical details of the UC. The concrete material parameters are: density $\rho_c = 2500\ kg/m^3$, Young's Modulus $E_c = 30\ GPa$ and Poisson's ratio $\nu_c = 0.2$. On the other hand, the bars that connect the pyramids are modeled using beam elements following Timoshenko theory (simulations are also performed with solid elements instead of beam elements, but give no significant differences in results). The material parameters are:

density $\rho_s = 7850\ kg/m^3$, Young's Modulus $E_s = 210\ GPa$ and Poisson's ratio $\nu_s = 0.3$. The phononic band structure of the structure in Fig. 1a is calculated implementing Bloch boundary conditions on the edges of the UC to account for the periodicity of the system [25]:

$$\vec{u}(\vec{r} + \vec{R}) = \vec{u}(\vec{r})e^{-i\vec{k}_F \cdot \vec{R}}, \tag{1}$$

where $\vec{u}$ represents the displacement vector, $\vec{R}$ is the lattice vector and $\vec{k}_F$ is the Bloch vector. Band structures are obtained by letting the wavevector $\vec{k}_F = (\vec{k}_{Fx}, \vec{k}_{Fy}, \vec{k}_{Fz})$ span selected points along the path of the Irreducible Brillouin Zone (IBZ) (Fig. 2). The main directions of symmetry in the reciprocal space $\Gamma X - XM - M\Gamma - \Gamma R - RX - XM - MR$ identify the 3D IBZ. The bandgap opening mode at $f_{bot} = 32.7$ Hz involves a large percentage of the total mass of the system, i.e., the mobilization of the concrete pyramids. The bandgap closing mode, at $f_{top} = 270.0$ Hz is characterized by the vibration of the steel beams instead of the concrete pyramids. The relative band gap width (in %) can be calculated as follows:

$$bandgap_{\%} = 2 \cdot \frac{f_{top} - f_{bot}}{f_{top} + f_{bot}} = 156.8\,\% \tag{2}$$

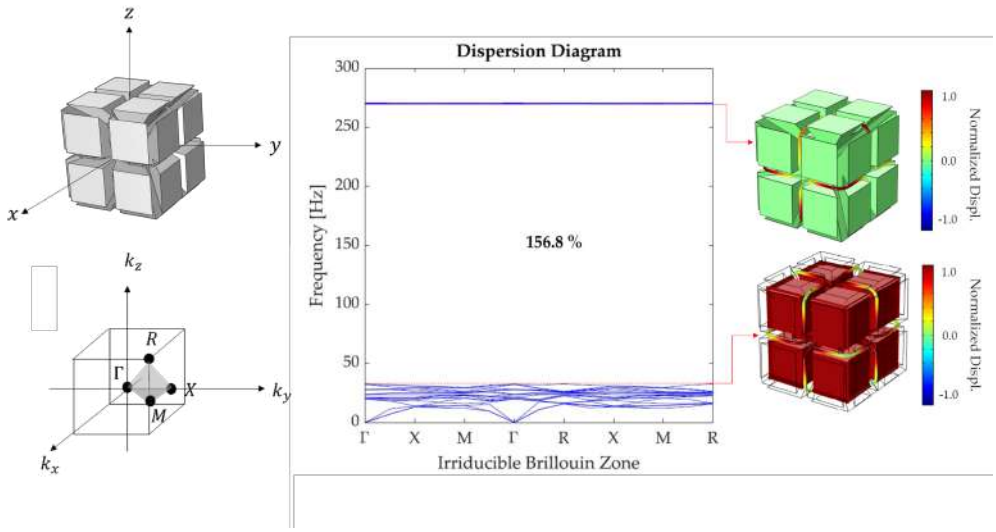

Figure 2: (Left) 3D view of the UC and schematic of its IBZ. (Centre) dispersion diagram of the periodic structure. (Right) eigenmodes of the UC corresponding to the f_{top} and f_{bot} eigenfrequencies, respectively.

3.2. Transmission Analysis of the UC

The FE model of the system is used to numerically evaluate its mechanical transmission, calculated as:

$$T = 20 \cdot log_{10}\left(\frac{A_{out}}{A_{in}}\right) \tag{3}$$

where A_{in} and A_{out} are the accelerations at the input and output areas, respectively. Input and output areas are chosen on opposite faces, as shown in Fig. 3; the input area is excited with a harmonic force with amplitude equal to 1 N and the resulting acceleration is detected at the output area A_{out}, carrying out a sweep frequency analysis. Results are consistent with band gap analysis, showing significant vibration attenuation between 35-250 Hz, which is the frequency range targeted in this study.

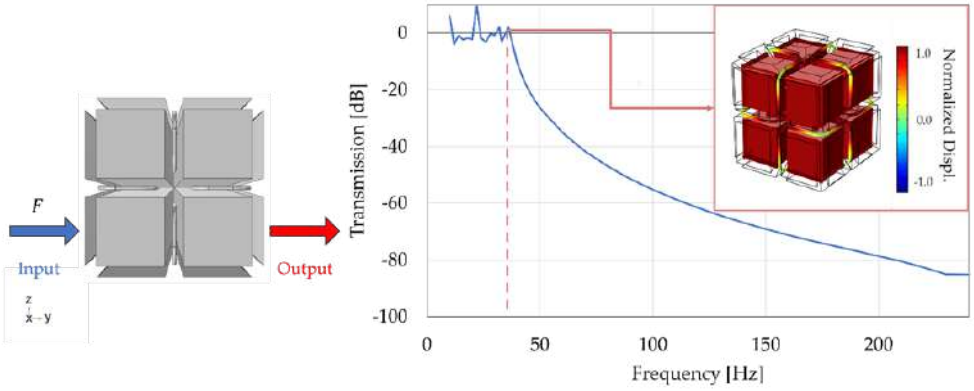

Figure 3: (Left) schematic of the input and output positions in the numerical model and (right) the numerically-calculated transmission spectrum together with the eigenmode at f_{bot} shown in the inset

4. UC Experimental Laboratory Tests

The mechanical transmission of the system is experimentally evaluated by means of a setup comprising an arbitrary waveform generator Agilent 33220A, able to perform frequency sweeps; a NI-9234 sound and vibration recording module and a NI cDAQ-9171 data acquisition module; a permanent magnet shaker LDS V406, generally used for modal and structural health monitoring (e.g. bridge testing); two PCB Piezotronics 353B15 (sensitivity of 10 mV/g, resonant frequency of 70 kHz) accelerometers. The range of frequencies in which the actuator has a flat response is from 5 Hz to 9 kHz, with a nominal peak sine rating of 98 N, and with a movable mass of 0.20 kg. The actuator head is placed at the centre of the UC (Fig. 4) in order to excite one of the lateral faces of the cube. The two accelerometers are positioned at two opposite faces, so that the input and output accelerations can be measured. The whole experimental setup is shown in Figure 4.

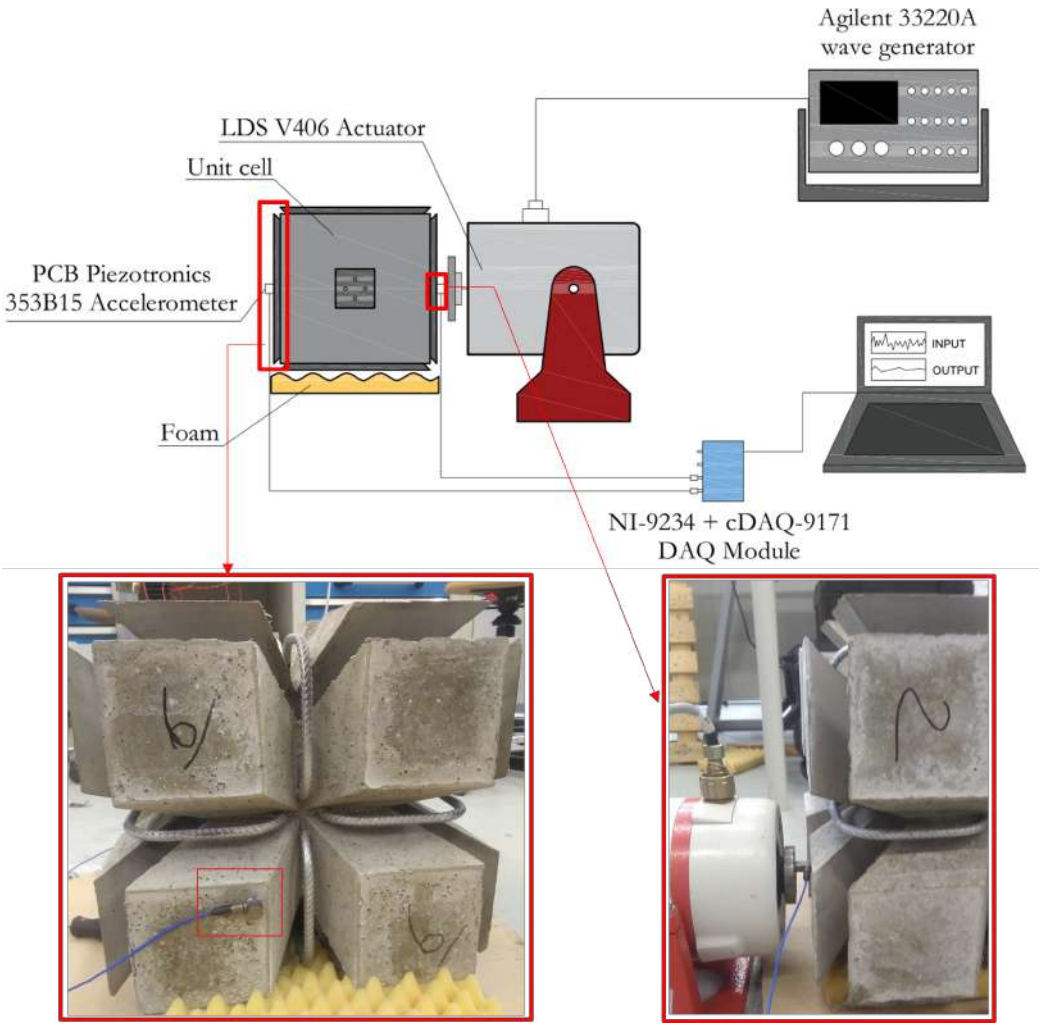

Figure 4: (Above) schematic of the experimental setup. (Below, from left to right) output side view (accelerometer position in red square), and input side view (shaker).

The experiment is performed by using a sine sweep actuation and measuring the corresponding output with the accelerometer. The transmission is computed as in Equation 3.

Figure 5 shows an excellent agreement between experimental and numerical transmission curves. In particular, the clear drop in transmission occurs after 32.5 Hz, which corresponds to the UC mode involving pyramidal masses and the steel beams acting as flexural elements, as described in Section 3.1.

The experimentally measured transmission appears constant above 100 Hz, as the acceleration amplitude is below the signal measurement noise.

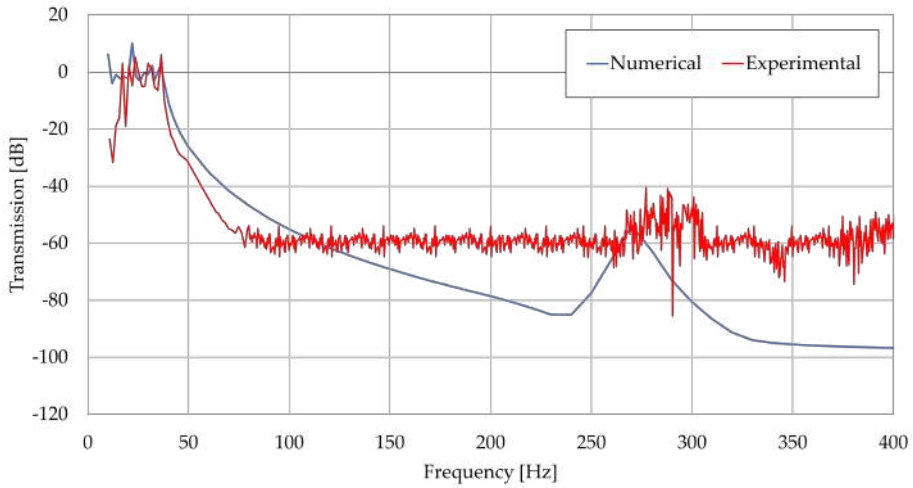

Figure 5: Comparison of the transmission curves obtained numerically and experimentally.

5. Design of Anti-Vibration Modules

The UC presented in previous sections is now used for a field test for the mitigation of railway induced vibrations. There are some problematic aspects when directly burying the UC in the ground, which may decrease its efficiency: for instance, a non uniform contact with the soil and a potential alteration of the dynamic behaviour of the cell because the soil can fill the gaps between the components (i.e., between the pyramid cement blocks) and modify the modes and frequencies of the resonators in an uncontrolled way. Moreover, direct application of the UC in the ground may lead to difficulties in installation and durability issues, since it would also assume a load bearing, as well as a vibration damping function.

To avoid these problems, an outer module which encloses the UCs is designed, ensuring a load-bearing function and uniform contact with the soil. The module is depicted in Figure 6, and consists of a U-shaped reinforced-concrete block enclosing a $3\times2\times1$ array of UCs. The resulting antivibration module is named "PhV-MQ-A" in the following, while the sole U-block is referred to as

"PhV-MQ-B". In the manufacturing phase, the UCs of the PhV-MQ-A are attached to the walls of the block through a thin film of epoxy resin applied on the external faces of the pyramids and the internal ones of the U-block. This ensures coupling and vibration transmission at the interfaces between elements. The resulting design of the anti-vibration module therefore allows:

- to protect the cells from the soil to preserve both their dynamic behaviour and durability;
- a more uniform pressure distribution across their flat lateral surfaces
- an easier transport and field installation.

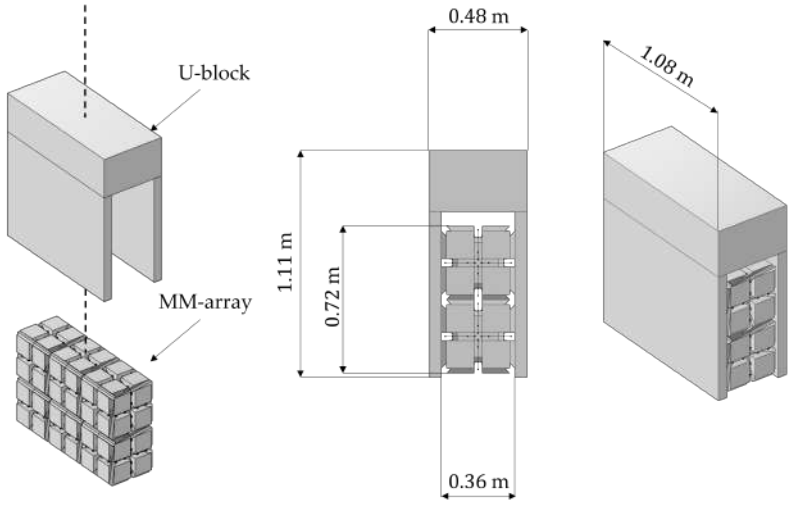

Figure 6: (From left to right) exploded, front-, and isometric- views of the anti-vibration module consisting of six UCs and a surrounding U-shaped concrete block. Main element dimensions are indicated.

The presence of the U-shaped block modifies the behaviour of the connected UCs, and numerical analysis is necessary to determine the vibration characteristics of the whole module.

6. Numerical Analysis of the Anti-Vibration Modules

Numerical analysis is performed on PhV-MQ-A and PhV-MQ-B structures to investigate the effect of the casing on the structure. A FE modal analysis is performed by introducing a harmonic unit input force $F = Ae^{i\omega t}$, with $A = 1$ N applied on one side of the U-block along its normal direction. On the same surface and on the opposite one, the average of the normal acceleration amplitude is calculated, and the transmission spectrum is then computed by using equation 3 both for PhV-MQ-A and PhV-MQ-B, as shown in Fig. 7a. The two spectra display two minima in transmission in the low frequency range ($5 - 45$ Hz) for PhV-MQ-A that are absent in PhV-MQ-B. These are associated with the "locally resonant" behavior of the structure [26]. The lowest minimum is attained at $f = 32.5$ Hz, which corresponds to the eigenfrequency of the MM. The other occurs at $f = 27.5$ Hz, which corresponds to another resonant mode of the MM. The largest transmission peak for PhV-MQ-A is attained at 45 Hz, which corresponds instead to a resonance mode in which the largest acceleration is concentrated in the U-block of the structure. 7b and 7c show that for both modal shapes, the two concrete walls of the U-block are rigidly coupled, and the system thus acts as a stiff barrier. Well beyond the resonance frequency, the walls are decoupled, and the system thus acts as a soft trench. At the resonance frequency however, the UCs vibrate and consequently absorb the vibration energy. This resonance is seen to take place at about 30 Hz. Additionally, it can be pointed out that the PhV-MQ-B (without UCs) does not display a resonance peak.

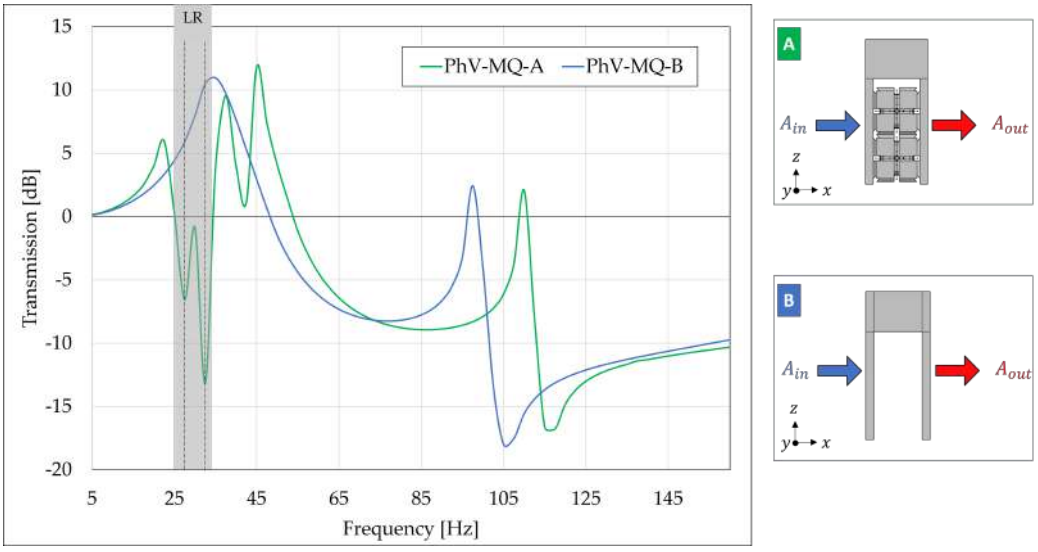

(a)

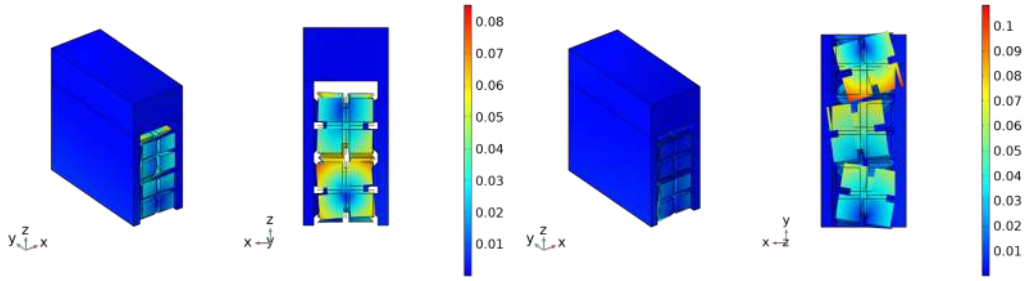

(b) (c)

Figure 7: (a) left, numerical transmission spectra of PhV-MQ-A and PhV-MQ-B. The shaded region occurs in the low-frequency range in which the transmission of the PhV-MQ-A falls below zero due to the locally resonant effect. The two dashed vertical lines are in correspondence with the resonant modes of the structure. Right, schematic of the models. (b) and (c) Acceleration magnitude (in m/s^2 represented in colour scale) of the resonant modes at 32.5 and 27.5 Hz.

7. Field Test

7.1. Test Site

Finally, the modules were tested in real conditions to validate their efficiency in mitigating railway-induced vibrations.

The testing site was located in Elze (see Figure 8a), in Germany. The Elze

train station of the Deutsche Bahn infrastructure is particularly suitable because of the presence of scarcely used track sections surrounded by sufficient space to allow for the installation and the testing in relevant environment (Figure 8b). The in-field tests were performed in two sessions, one for each of the two setups, which comprised 40m-long trench barriers where modules PhV-MQ-A and then -B were installed. In particular, the installation of the solution PhV-MQ-B was aimed to separate the effect of the UCs from that of the concrete U-shaped super-structure.

(a)

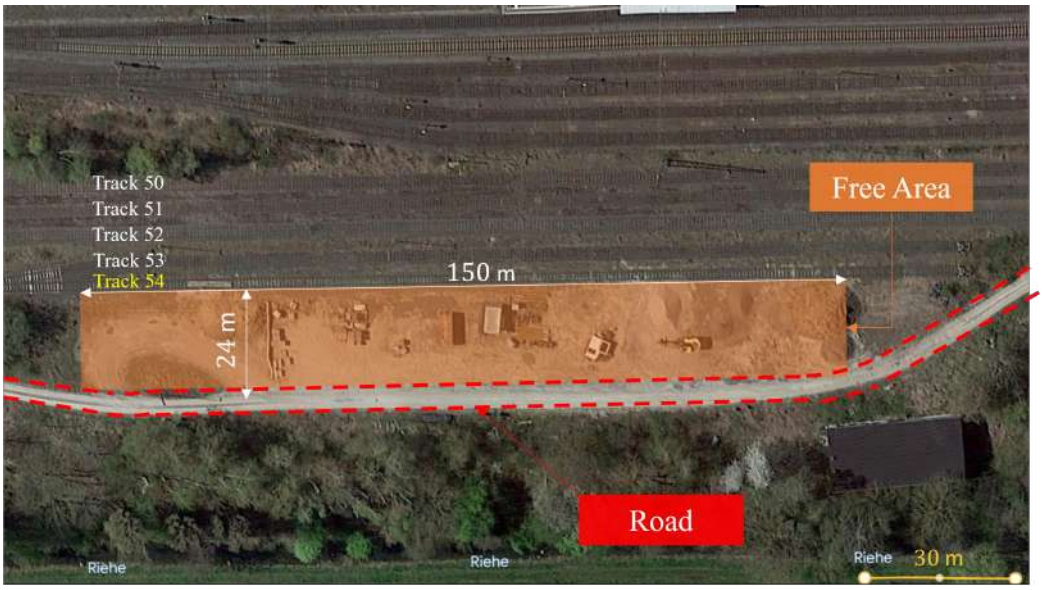

(b)

Figure 8: (a) Satellite picture of Elze and of its main railway station, in which the dashed lines highlight the installation site. (b) View of the installation site.

7.2. Measurement Setup

Measurements were carried out by Baudynamik Heiland & Mistler GmbH [27] on the $11^{th} - 12^{th}$ May (baseline prior to the installation of the modules) and on the 18^{th} June 2020 (after installation).

The goal was to first determine the transfer function of the soil, i.e., soil mobility, with and without the anti-vibration solution. Mobility measurements were performed by means of an artificial (drop weight) excitation. The comparison between mobility measurements performed before and after the installation of the anti-vibration elements allowed to obtain the Insertion Loss (IL) provided by the anti-vibration modules. The mobility is computed from the measurement of the vibration velocity arising from a known input force. A drop weight excitation was used at several impact points on the track while the vibration response was recorded at several points beyond the anti-vibration modules. The location of the impact source and the output sensors varied, so that we will refer to a transfer mobility, which is dependent on the distance, the soil conditions and the type of excitation (point or line source).

A DYNPACT® excitation source was used, i.e., a device that drops a 50 kg weight from a height of 1 m (see Figure 9).

Figure 9: DYNPACT® excitation source used for the measurements.

This induces a pulse-shaped force in the ground that propagates to the load cell location, whose amplitude depends on subsoil stiffness. The proper coupling of the load cell with the subsoil is obtained by a load-distributing

steel plate on a sand pad of 3 cm thickness. Before starting the measurements, several impacts were applied to avoid local compacting effects of the upper soil layers. The excitation was performed on the track bed between the rail profiles. A schematic of the impact and measuring point locations is shown in Fig. 10.

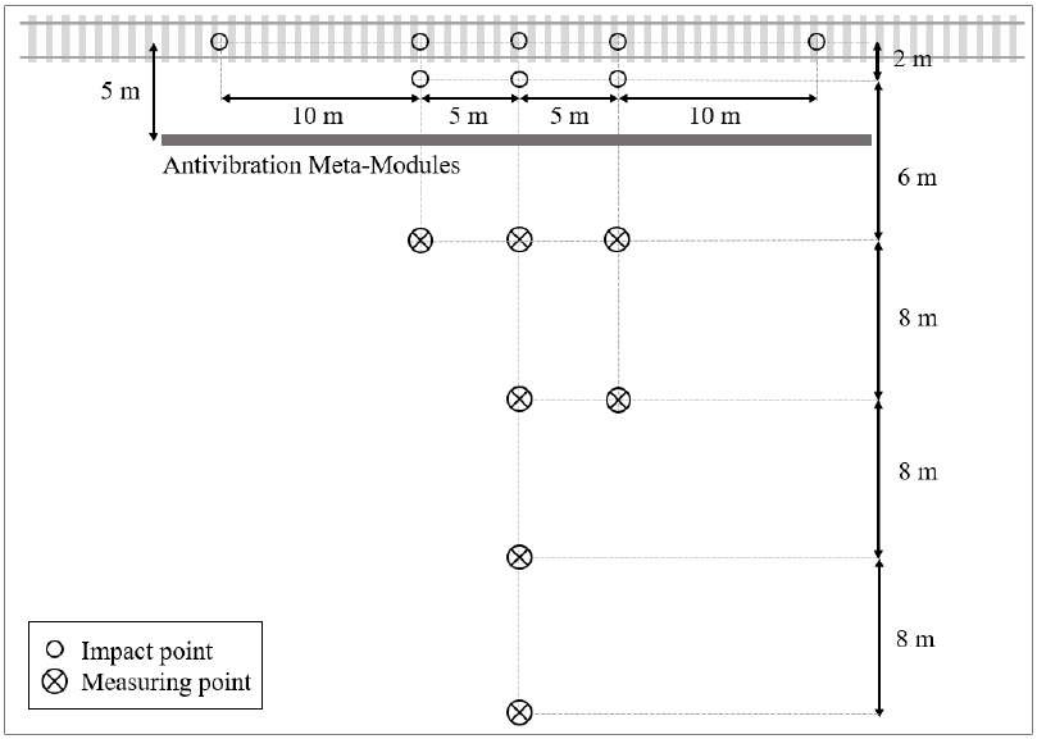

Figure 10: Schematic of the experimental setup.

Vibration measurements were performed with geophones, which record the vibration velocity at the installation location. These were placed at 8, 16, 24, and 32 m from the center of the tracks, and kept in the same position for the measurements before and after antivibration meta-module installation, through the use of a sensor bed made of rapid hardening cement.

7.2.1. Soil characterization

In order to obtain information about the soil dynamic properties, additional sets of measurements were performed [27]. First, a measuring chain with horizontal geophones in the radial direction, i.e. perpendicular to the tracks, were installed, while vibrations in the soil were induced in the vertical direction by a hammer impact. Secondly, a similar measuring chain was set up with horizontal geophones oriented in the transversal direction, i.e. parallel to the track, while the soil excitation was performed in the horizontal direction, perpendicular to the measurement chain line, with a hammer impact. The recorded data on surface vibration waves were analysed with the Multichannel Analysis of Surface Waves (MASW) method. This method is based on the fact that the waves produced by the hammer impact are modified according to the properties of the soil medium during their propagation. By measuring these dispersion properties at different distances from the vibration source, the different layers of the soil (soil profile) can iteratively be reconstructed. For a more detailed description of the MASW method, see [28, 29].

Each layer is described by two parameters: the Shear Wave Velocity v_s and the Dynamic Shear Modulus G_{dyn}: results are illustrated in Figure 11.

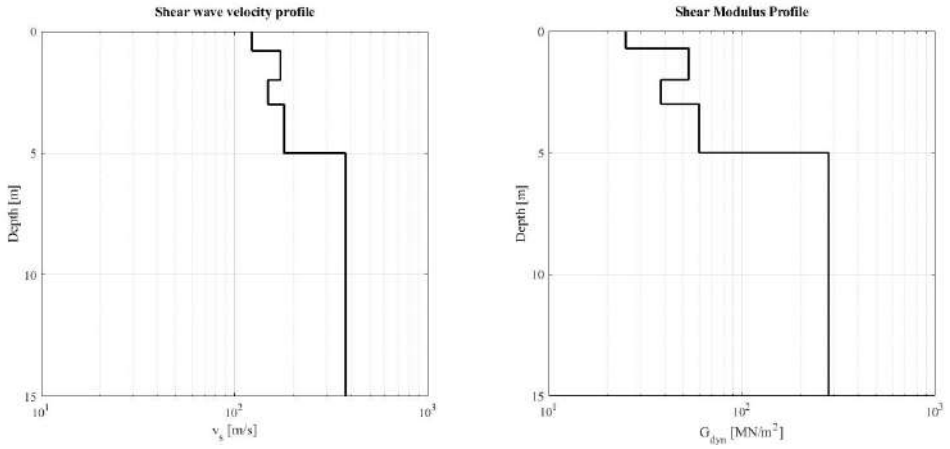

Figure 11: Results of the MASW analysis: soil profile in terms of shear wave velocity and dynamic shear modulus.

7.3. Results

In the following section, the main steps in the evaluation of the mobility transfer functions and of the IL are presented. Two excitation conditions are discussed: a point source and a line source excitation.

7.3.1. Point Source Excitation

Starting from the measurement setup described in Section 7.2 and in [27], the transfer functions are calculated for any combination of impact and measuring points as follows:

$$TF^{mnp}(f) = \frac{S^{p}_{A,m}(f) \cdot S_{E,n}(f)^{*}}{S_{E,n}(f) \cdot S_{E,n}(f)^{*}}, \tag{4}$$

where, $S^{p}_{A,m}(f)$ is the Fourier Transform of the vibration velocity measured at a distance p from the barrier and sampled by the m-th geophone. $S_{E,n}(f)$ is the Fourier Transform of the vibration velocity measured at the n-th impact point. The symbol $*$ denotes the complex-conjugate. To average the effect of distance and soil heterogeneities, the TF is used to compute a transfer mobility function as follows:

$$TM^{p}(f) = \frac{1}{M} \cdot \frac{1}{N} \sum_{m=1}^{M} \sum_{n=1}^{N} |TF^{mnp}(f)|^{2}, \tag{5}$$

where M is the number of geophones located at a distance p and N are the impact points, respectively.

For the computation of spectra, a force amplitude measurement trigger was set to $F_{trig} = 15\ kN$ with a pre-trigger time set to $0.1\ s$. Rectangle windowing was performed both on the excitation and response signals, with a window length of 4096 points and a sampling of 2560 Hz. The narrow-band transfer mobility functions are thus obtained with a frequency resolution of $\Delta f = 1/1.6\ s = 0.625\ Hz$, and then transformed into equivalent functions related to the 1/3 octave band frequencies. Finally, the IL at different distances from the source is calculated as:

$$IL(f) = 10log_{10}\left[\frac{TM^{p}_{0}(f)}{TM^{p}(f)}\right], \tag{6}$$

where $TM^{l}_{0}(f)$ is the transfer mobility function computed at a distance p from the input source before the installation.

Figs. 12a and 12b show a comparison of the IL spectra measured at at 8, 16, 24, and 32 m from the point source excitation for the PhV-MQ-A and PhV-MQ-B structures, respectively. For both modules, the IL is close to zero up to the 20 Hz frequency band (grey region), due to the small depth of the barrier [3]. Within the frequency bands from 20 to 50 Hz (red region) the modules present different behaviours. For the PhV-MQ-A, a maximum around 10 dB is attained at 31.5 Hz and preserved along the whole distance. This implies that the energy propagating within this frequency range is not transmitted across the barrier, but absorbed through the mechanism of local resonance. The PhV-MQ-B instead, presents two peaks around 8 dB at 25 and 40 Hz bands that rapidly decay below 2 dB with distance. More quantitatively, the PhV-MQ-A solution displays an increment in IL in the 31.5 Hz frequency band due to UC resonance of 6 dB with respect to the PhV-MQ-B solution at 8m from the source. The increment reaches up to 8.5 dB at 32 m from the excitation source. The overall vibration mitigation provided by the PhV-MQ-A solution with respect to the baseline (before installation) is observed in the frequency range 20-50 Hz (red transparency region) with peak values of 10 dB.

Thus, due to its small depth, the U-shaped module (PhV-MQ-B) is only capable of influencing the vibration propagation near the stiff barrier, but its effect strongly decays with distance. This is compatible with the so-called "wave healing" phenomenon which tends to reduce the scattering effect with the distance on both amplitude and phase from weak scatterers. Moreover, previous studies have demonstrated that in stratified soils, Rayleigh waves redirected to the soil tend to re-surface because of the increasing depth dependent velocity (mirage effect) [30, 31]. Instead, the U-shaped barrier with embedded metamaterial resonators (PhV-MQ-A) is effective in attenuating vibrations at all considered distances in the designed frequency range, demonstrating a considerable advantage. Experimental results are also consistent with full-field wave propagation simulations in the soil, reported in the Supplementary Material. Although at least from a qualitative point of view, experimental results confirm numerical predictions, the latter provide a forcibly simplified picture of the wave propagation problem, since it is difficult to choose realistic soil-structure interaction conditions as well as a correct model for soil viscoelasticity. However, we emphasize that the objective of this paper is not to compare experimental results to numerical simulations, but to provide a direct in-field experimental verification of the designed barriers.

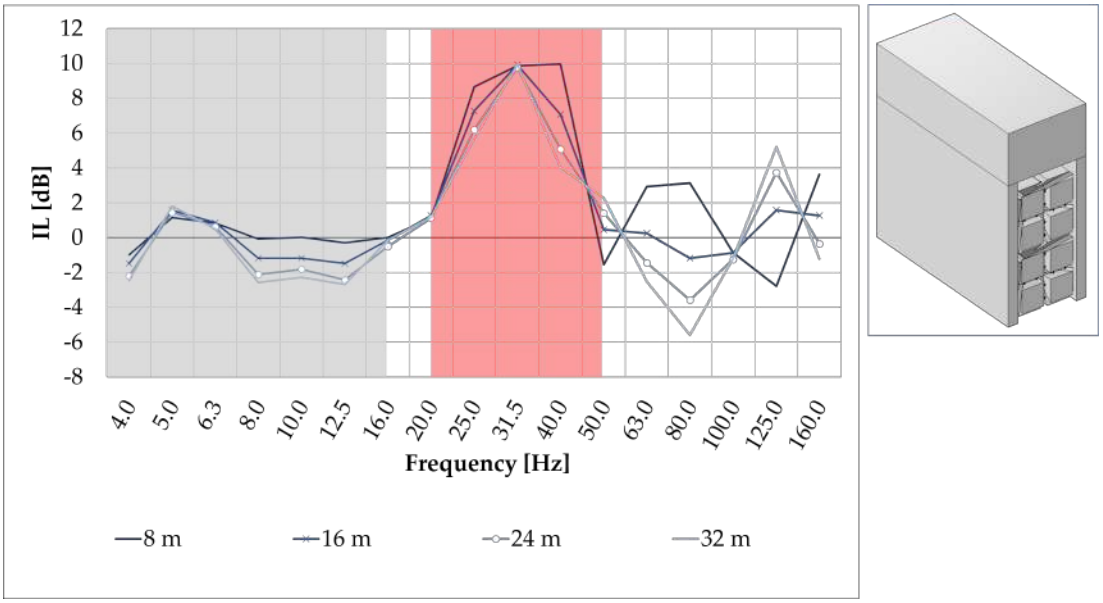

(a)

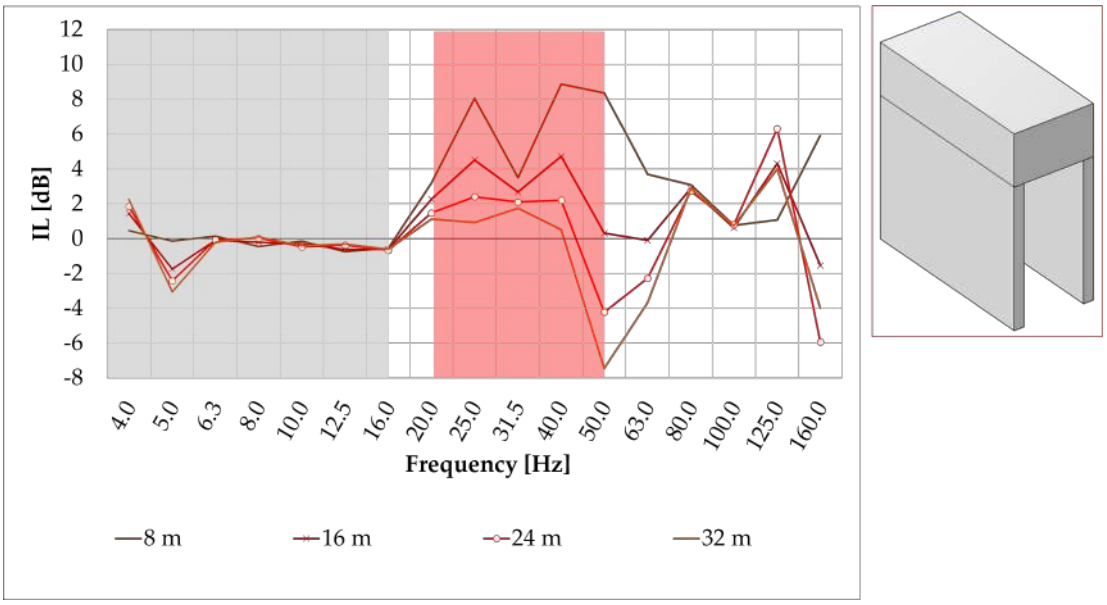

(b)

Figure 12: Point Source. Comparison of the IL at different distances from the source for (a) the solution PhV-MQ-A and (b) the solution PhV-MQ-B. The red shaded region indicates the frequency range in which the two UC types differ in spectral behaviour

7.3.2. Line Source Excitation

The mobility functions computed in the previous section for each point source can be conveniently transformed by integration into mobility functions for a line source excitation, which is more representative of the real working conditions, namely the train excitation.

First of all, for each frequency band of the spectrum, a regression analysis is performed on the results in terms of transfer mobility functions for point sources. This regression analysis is based on the assumption of an exponential decay of the transfer mobility with distance d:

$$TM^l(f,d) = TM^p(f) \cdot \left(\frac{d_0}{d}\right)^{n_P(f)}, \tag{7}$$

where TM^l is the line transfer mobility, $d_0 = 8$ m and $n_P(f)$ quantifies the vibration decay with distance, which is computed as a regression value which fits the mobility decay with distance at a specific frequency band, as described in [32]. The line source transfer mobility function can then be computed at desired locations, integrating the transfer mobility functions generated for several point sources obtained at the previous step with the corresponding influence length (fig. 13). It is important to underline that a line source has a shorter distance decay coefficient that a point source. Results indicate that the following relation holds:

$$n_L = n_P + 0.5. \tag{8}$$

where n_L quantifies the line mobility decay.

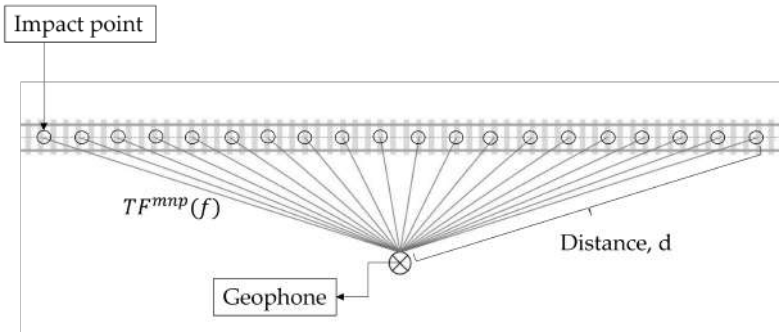

Figure 13: Schematic representation of the construction of a line source from point sources, to obtain the line source mobility functions at a desired location by integrating point transfer mobility functions.

As has been described for the case of point source, the IL can be obtained from the mobility transfer functions at the desired locations as the difference between the transfer mobility before and after the installation of the proposed solutions. The comparison of ILs at 8 m, 16 m, 24 m and 32 m from the line excitation source between the PhV-MQ-A and PhV-MQ-B is shown in Fig. 14a and 14b, respectively. A similar interpretation of the results for a line source can be made as in the case of a point excitation. Here too, the resonance effect of the UCs leads up to a 6 dB of IL gain in the frequency bands $20 - 40$ Hz, compared to the PhV-MQ-B. The overall vibration insulation effect of PhV-MQ-A is stable with distance and reaches up to 10 dB of mitigation.

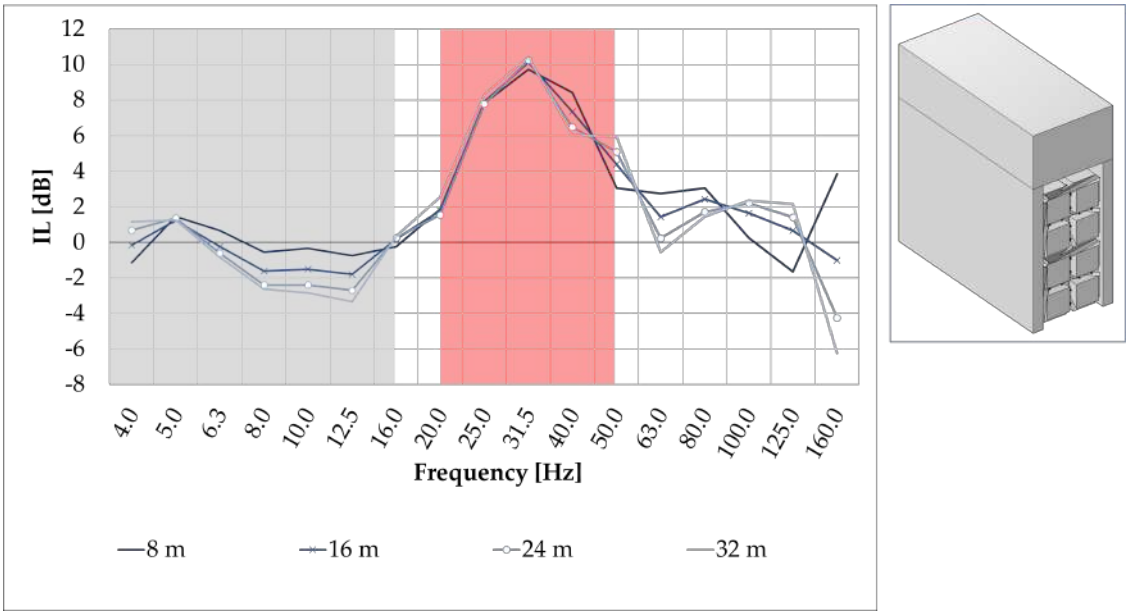

(a)

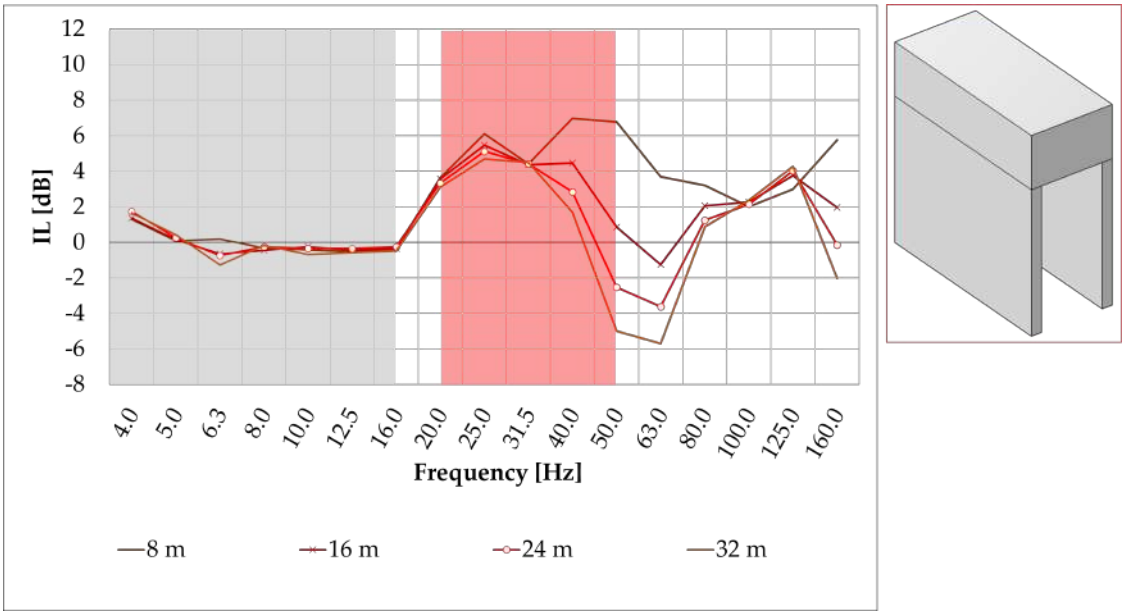

(b)

Figure 14: Line Source. Comparison of the IL at different distances from the source for the solution PhV-MQ-A (a) and for the solution PhV-MQ-B (b). The red shaded region indicates the frequency range in which the two UC types differ in spectral behaviour

8. Conclusions

In this work, the process of design and validation in relevant environment of a MM-based modular panel for vibration mitigation in soils was performed. The MM UC was optimized to improve vibration insulation in the desired frequency range (30 Hz), exploiting its low frequency resonance. Its efficiency was firstly evaluated in numerical and experimental laboratory tests. A concrete U-block encasement was developed to decouple the MM structure form the soil, in order to allow its vibration at resonance frequency. The design of the structure was then validated by means of FEM analysis. Then, a field experimental campaign for its validation was performed: the MM-based modular panel was installed and tested at a railway station site under an artificial excitation to investigate its effect of mitigation of railway-induced vibrations. An IL of up to 10 dB was obtained in the low frequency range (20-50 Hz), in accordance with numerical simulations, and presented in addition a stable insulation measured up to 32 m from the track. Further improvements in the working conditions can probably be obtained with better consolidation and settlement of the soil in the trench around the barrier to improve contact conditions and homogenise the soil properties in the vicinity of the barrier. Moreover, the application of a geotextile within the trench could prevent the soil from spreading inside the cavities of the metabarrier modifying the resonance modes and possibly leading to performance degradation. This work demonstrates the feasibility of using metamaterial solutions for the reduction of low frequency groundborne vibrations such as those emitted by rail traffic. This can constitute an attractive solution, given the non-invasive installation below surface, removed from the rails, the limited size (1 m depth) and realization using conventional building materials.

9. Acknowledgements

The results presented in this paper have been obtained and supported within the framework of the DB mindbox ConTech startup program for innovation, as well as the European Union's Horizon 2020 FET Open ("Boheme") project under grant agreement No. 863179. A grateful thanks is due to Mr Frank Limprecht, Head of North Infrastructure Projects at DB Netze AG, as well as Baudynamik Heiland & Mistler GmbH for their fundamental contribution in the in-situ experimental campaign.

References

[1] S. Ouakka, O. Verlinden, G. Kouroussis, Railway ground vibration and mitigation measures: benchmarking of best practices, Railway Engineering Science 30 (1) (2022) 1–22.

[2] P. Coulier, V. Cuellar, G. Degrande, G. Lombaert, Experimental and numerical evaluation of the effectiveness of a stiff wave barrier in the soil, Soil Dynamics and Earthquake Engng. 77 (1) (2015) 238–253.

[3] A. Dijckmans, A. Ekblad, A. Smekal, G. Degrande, G. Lombaert, Efficacy of a sheet pile wall as a wave barrier for railway induced ground vibration, Soil Dynamics and Earthquake Engng. 84 (1) (2016) 55–69.

[4] L. Jae-Hwang, J. P. Singer, E. L. Thomas, Micro-/nanostructured mechanical metamaterials, Advanced materials (2012).

[5] K. Bertoldi, V. Vitelli, J. Christensen, M. V. Hecke, Flexible mechanical metamaterials, Nature Reviews Materials (2017).

[6] J. U. Surjadi, L. Gao, H. Du, X. Li, X. Xiong, N. X. Fang, Y. Lu, Mechanical metamaterials and their engineering applications, Advanced Engineering Materials (2019).

[7] M. Guancong, P. Sheng, Acoustic metamaterials: From local resonances to broad horizons, Science advances (2016).

[8] S. Sadat-Saleh, S. Benchabane, F. I. Baida, M.-P. Bernal, V. Laude, Tailoring simultaneous photonic and phononic band gaps, Journal of Applied Physics (2009).

[9] Z. Liu, X. Zhang, Z. Mao, Y. Zhu, Z. Yang, C. Chan, P. Sheng, Locally resonant sonic materials, Science 289 (1) (2000) 1734–1736.

[10] V. Laude, Phononic crystals, in: Phononic Crystals, de Gruyter, 2020.

[11] A. O. Krushynska, M. Miniaci, F. Bosia, N. M. Pugno, Coupling local resonance with bragg band gaps in single-phase mechanical metamaterials, Extreme Mechanics Letters 12 (2017) 30–36.

[12] H. M. van Driel, W. L. Vos, Multiple bragg wave coupling in photonic band-gap crystals, Physical Review B 62 (15) (2000) 9872.

[13] B. R. Mace, E. Manconi, Wave motion and dispersion phenomena: Veering, locking and strong coupling effects, The Journal of the Acoustical Society of America 131 (2) (2012) 1015–1028.

[14] E. Manconi, B. Mace, Veering and strong coupling effects in structural dynamics, Journal of Vibration and Acoustics 139 (2) (2017) 021009.

[15] A. Castanheira-Pinto, P. Alves-Costa, L. Godinho, P. Amado-Mendes, On the application of continuous buried periodic inclusions on the filtering of traffic vibrations: A numerical study, Soil Dynamics and Earthquake Engineering 113 (2018) 391–405.

[16] L. Lei, L. Miao, C. Li, X. Liang, J. Wang, Locally resonant periodic wave barriers for vibration isolation in subway engineering, KSCE Journal of Civil Engineering 25 (2021) 1239–1251.

[17] A. Palermo, S. Krödel, A. Marzani, C. Daraio, Engineered metabarrier as shield from seismic surface waves, Scientific reports (2016).

[18] M. Miniaci, A. Krushynska, F. Bosia, N. M. Pugno, Large scale mechanical metamaterials as seismic shields, New Journal of Physics 18 (8) (2016) 083041.

[19] Y. Achaoui, T. Antonakakis, S. Brûlé, R. Craster, S. Enoch, S. Guenneau, Clamped seismic metamaterials: ultra-low frequency stop bands, New Journal of Physics 19 (6) (2017) 063022.

[20] D. Colquitt, A. Colombi, R. Craster, P. Roux, S. Guenneau, Seismic metasurfaces: Sub-wavelength resonators and rayleigh wave interaction, Journal of the Mechanics and Physics of Solids 99 (2017) 379–393.

[21] A. Colombi, D. Colquitt, P. Roux, S. Guenneau, R. V. Craster, A seismic metamaterial: The resonant metawedge, Scientific reports 6 (1) (2016) 27717.

[22] A. Colombi, P. Roux, S. Guenneau, P. Gueguen, R. V. Craster, Forests as a natural seismic metamaterial: Rayleigh wave bandgaps induced by local resonances, Scientific reports (2016).

[23] L. D'Alessandro, E. Belloni, R. Ardito, F. Braghin, A. Corigliano, Mechanical low-frequency filter via modes separation in 3d periodic structures, Applied Physics Letters (2017).

[24] L. D'Alessandro, R. Ardito, F. Braghin, A. Corigliano, Low frequency 3d ultra-wide vibration attenuation via elastic metamaterial, Scientific Reports (2019).

[25] V. Laude, Phononic Crystals: Artificial Crystals for Sonic, Acoustic, and Elastic Waves, De Gruyter, (2015).

[26] J. M. De Ponti, J. M. De Ponti, Graded elastic metamaterials, Graded Elastic Metamaterials for Energy Harvesting (2021) 61–89.

[27] P. D. Villamil, M. Mistler, F. Korda, Baudynamik Heiland & Mistler, Phononic Vibes, Elze test area: Measurement report and evaluation of the insertion loss resulting from the installation of metamaterial elements, report no. 80-10634-01-D1 (internal report on behalf of DB netz AG), Tech. rep. (2020).

[28] G. Dal Moro, Onde di superficie in geofisica applicata. Acquisizione e analisi di dati secondo tecniche MASW e HVSR., Flaccovio Dario, 2014.

[29] J.-S. L'Hereux, M. Long, Relationship between shear-wave velocity and geotechnical parameters for norwegian clays, J. Geotech. Geoenviron. Engng. 143 (6) (2017) 1.

[30] R. Zaccherini, A. Colombi, A. Palermo, V. K. Dertimanis, A. Marzani, H. R. Thomsen, B. Stojadinovic, E. N. Chatzi, Locally resonant metasurfaces for shear waves in granular media, Phys. Rev. Appl. 13 (2020) 034055.

[31] R. Zaccherini, A. Palermo, A. Marzani, A. Colombi, V. Dertimanis, E. Chatzi, Mitigation of rayleigh-like waves in granular media via multilayer resonant metabarriers, Applied Physics Letters 117 (25) (2020).

[32] A. Quagliata, M. Ahearn, E. Boeker, C. Roof, L. Meister, H. Singleton, Transit noise and vibration impact assessment manual, Tech. rep. (2018).